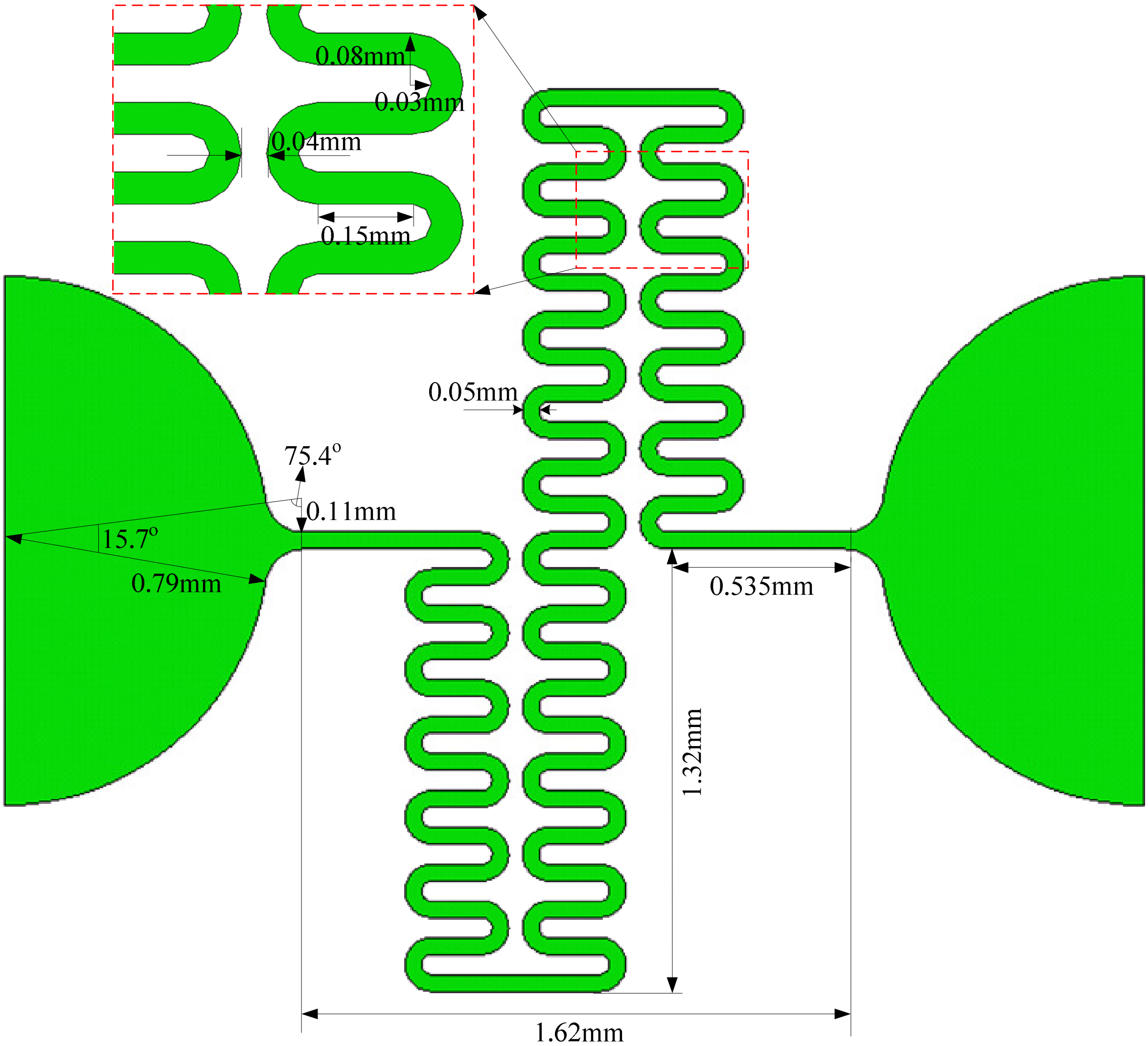

Supplementary Figure S1 | Illustration of the dimensions for the self-similar interconnect (copper layer). A representative unit cell of the self-similar serpentine interconnect is demonstrated in the figure.

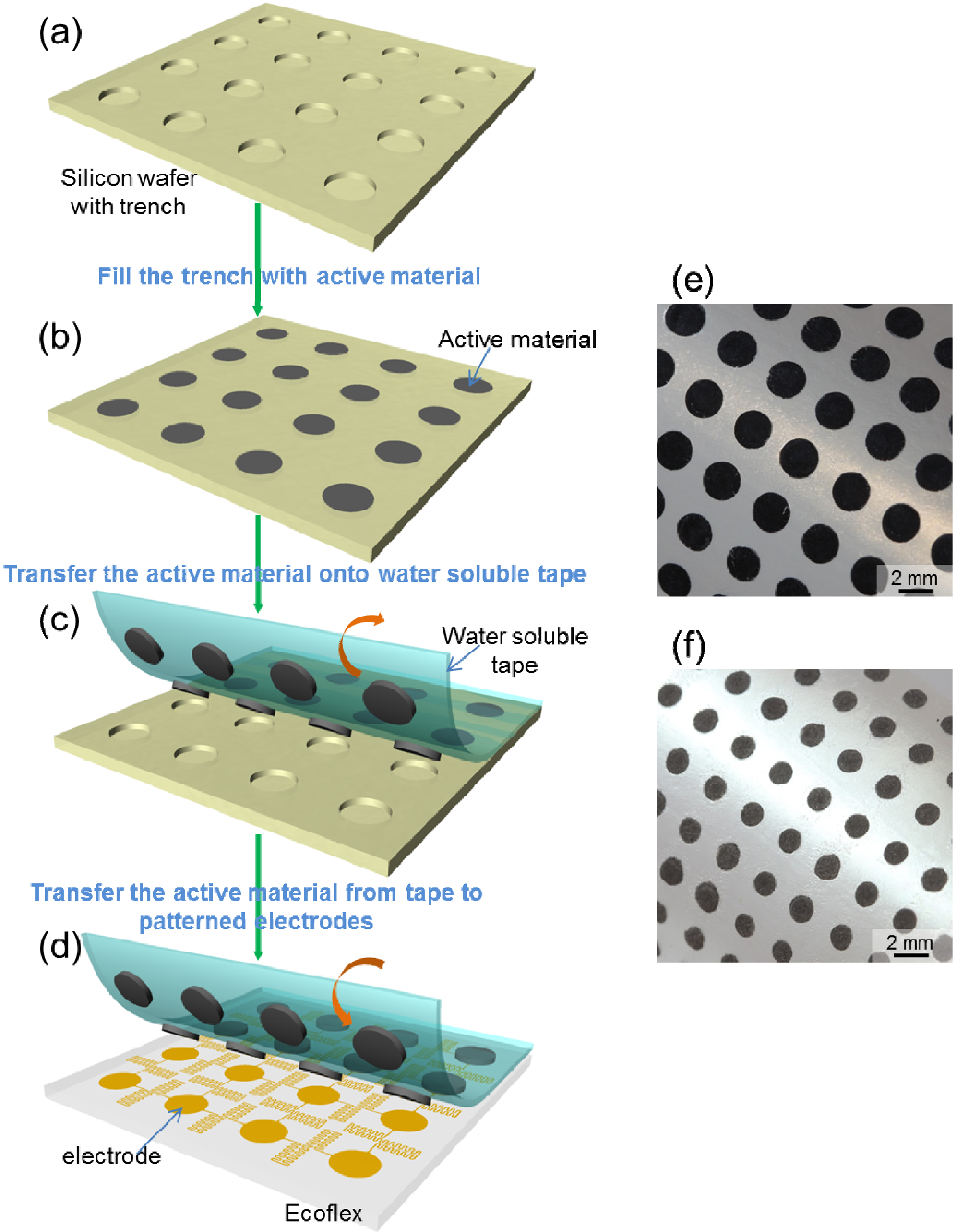

Supplementary Figure S2 | Schematic illustration of the fabrication process and the images of moulded slurries. (a)-(d) Schematic illustration of the transfer printing process, and images of the moulded (e) cathode and (f) anode slurry on water soluable tape.

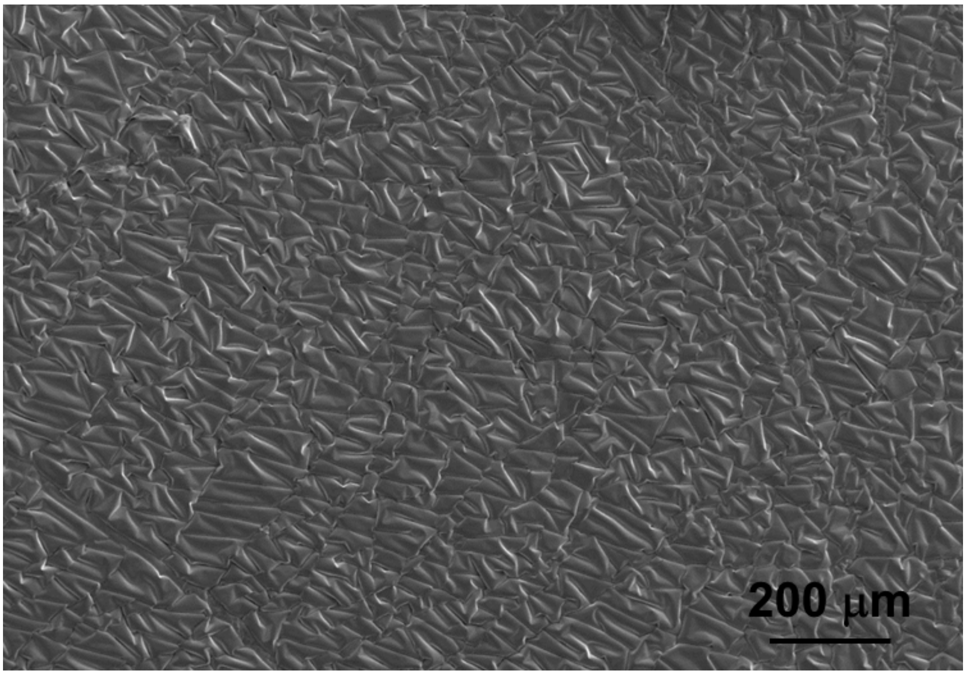

Supplementary Figure S3 | SEM image of a buckled Al foil (600 nm)/PI (1200 nm) bilayer on the surface of a sheet of ecoflex after releasing a prestrain of ~ 30%. This bilayer structure resembles the types of laminated Al/polymer packaging materials that are used in pouch cells, to block the permeation of water, air and solvent.

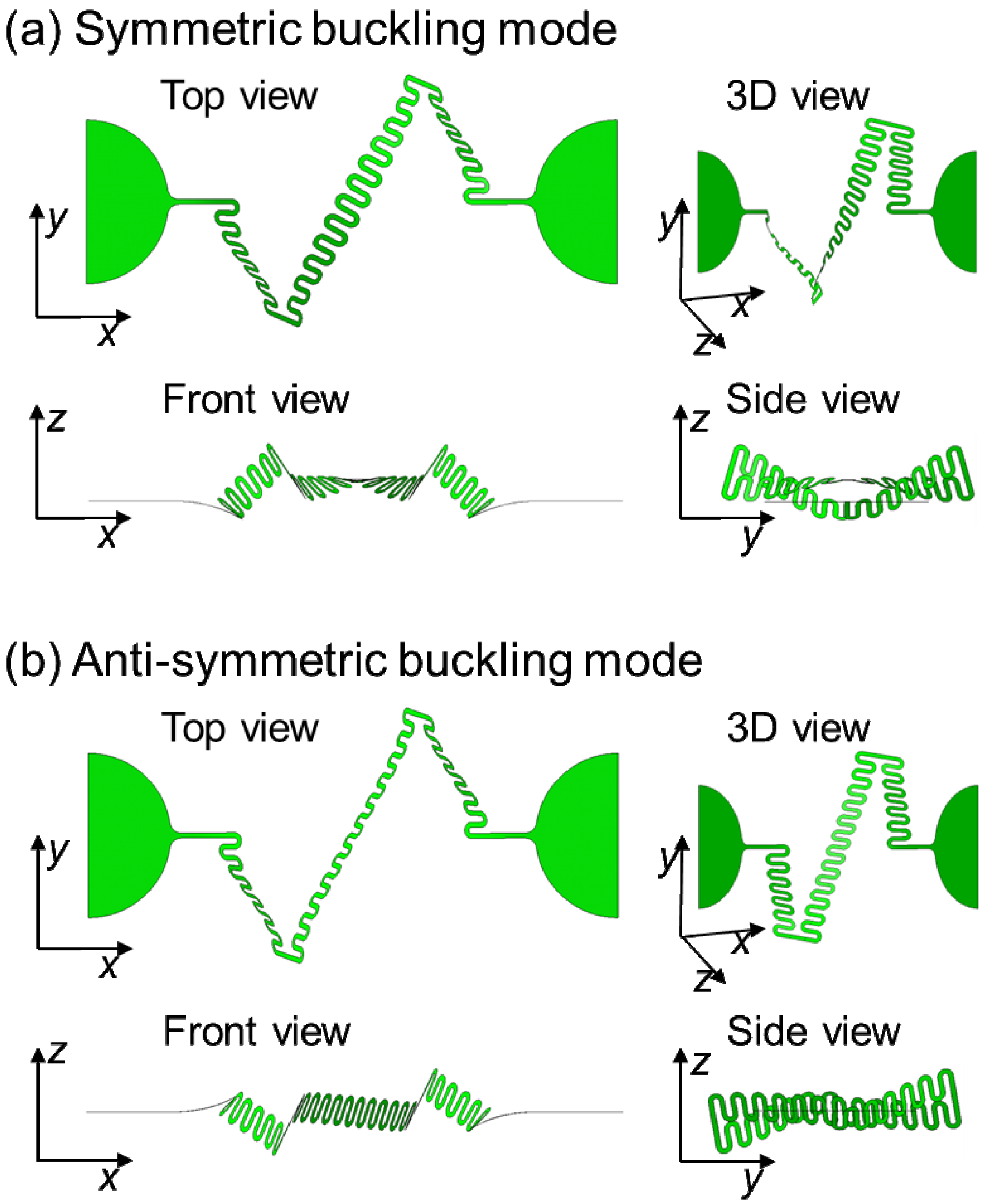

Supplementary Figure S4 | Deformed configurations (FEA results) of the self-similar electrodes. The structural configurations for symmetric (a) and anti-symmetric (b) buckling modes under an applied strain of 50%, from different viewing angles (i.e., top, front, side, and three-dimensional (3D) views).

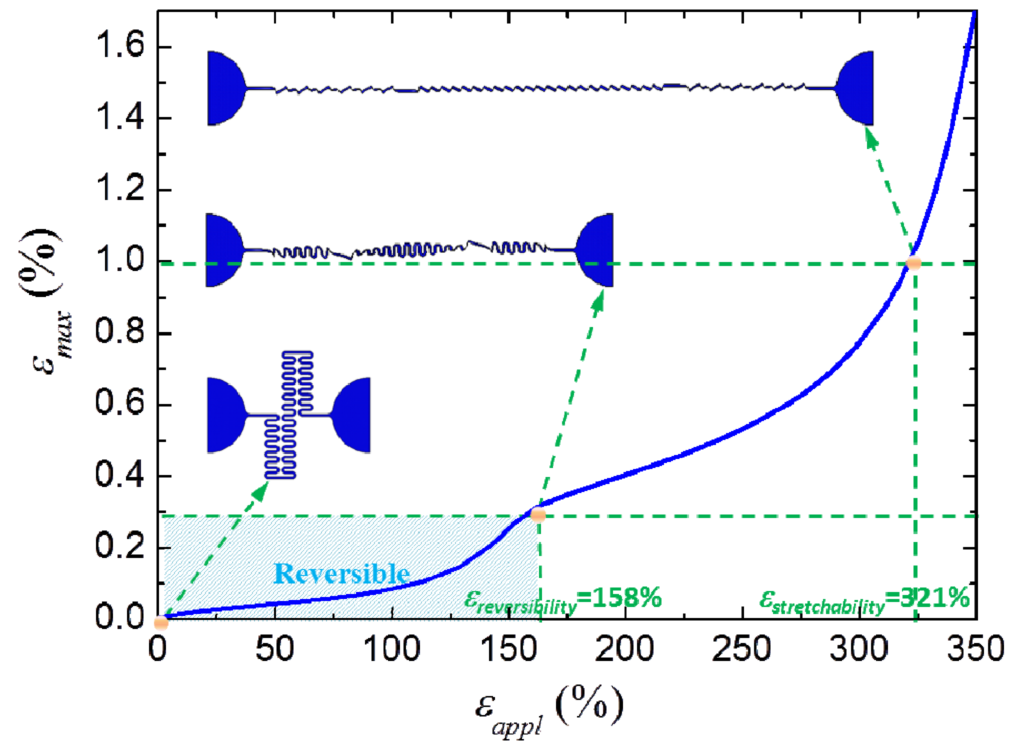

Supplementary Figure S5 | Dependence of metal strain (on the material level) on the applied strain (on the structural level). The maximum value (e_{max}) of the maximum principal strain in the metal layer of the self-similar interconnect is plotted as a function of the applied strain (e_{appl}), together with the evolution of the deformations.

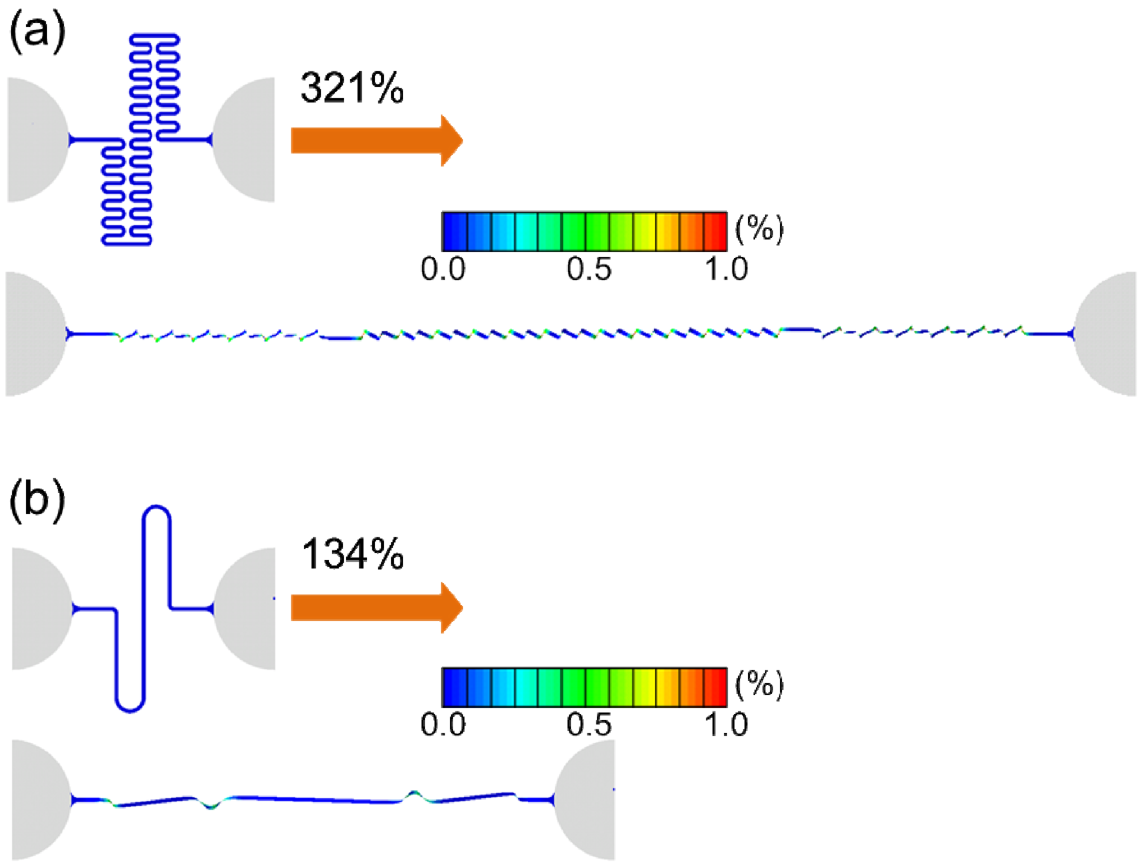

Supplementary Figure S6 | The distribution of maximum principal strain in the metal layer when its maximum value reaches 1%. (a) shows the results for the 2-order self-similar interconnect, and (b) is for the 1-order interconnect. The two structures have the same overall dimensions, and cross-sections.

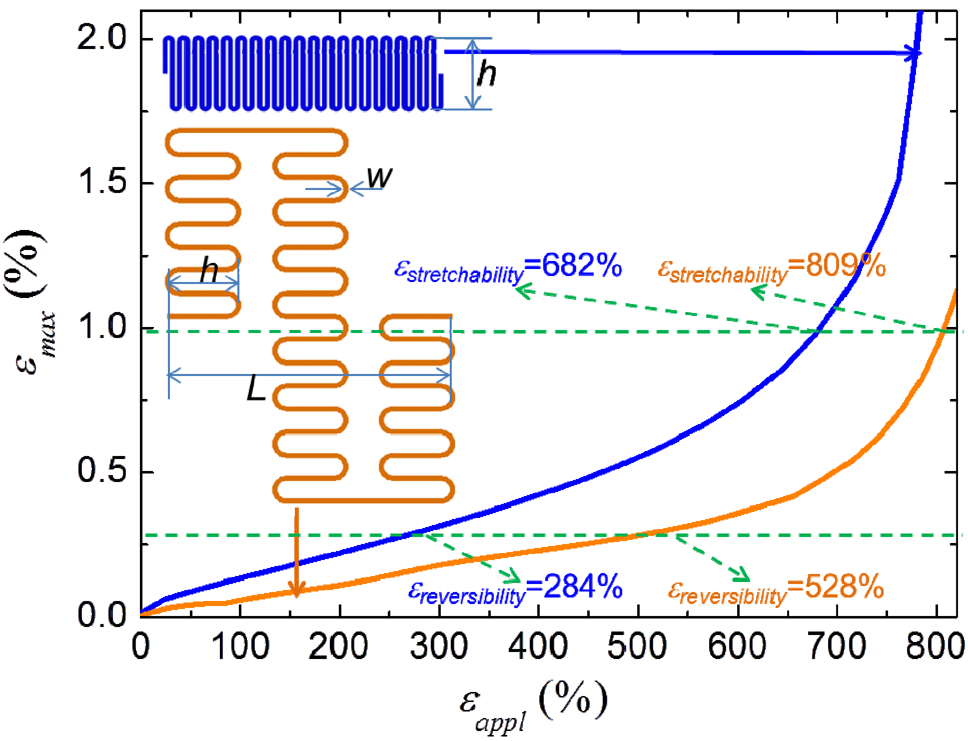

Supplementary Figure S7 | Comparison of metal strain level for the self-similar and simple serpentine designs. The maximum value (e_{max}) of the maximum principal strain in the metal layer of the interconnect is plotted as a function of the applied strain (e_{appl}). The two interconnects have the same total length (l_{total}), span (L), amplitude (h), width (w), and thickness (t).

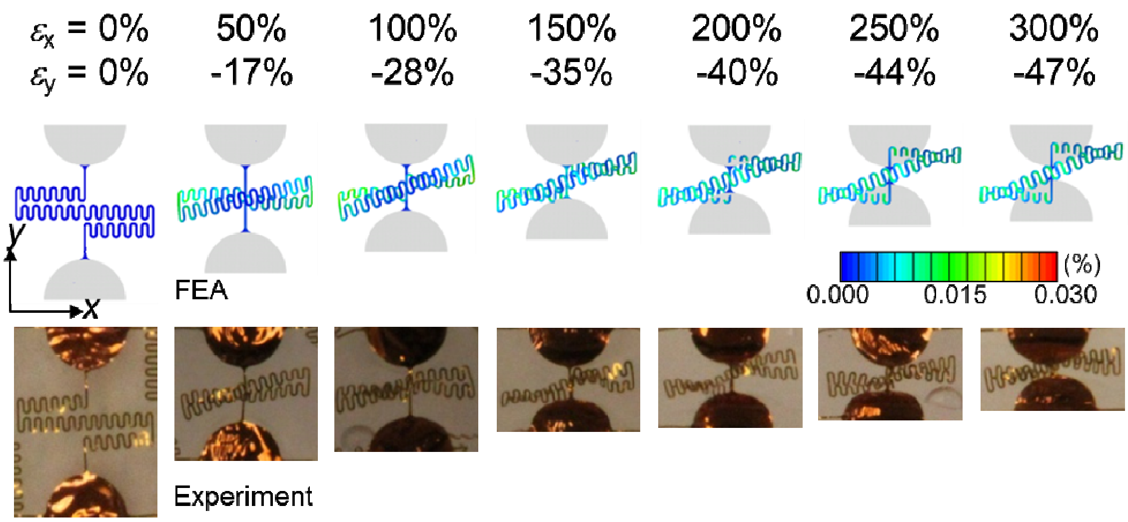

Supplementary Figure S8 | Finite element analyses and optical images of the buckling profiles of a vertically aligned self-similar interconnect under compression. The color contours in the FEA results represent the distribution of maximum principal strain in the metal layer.

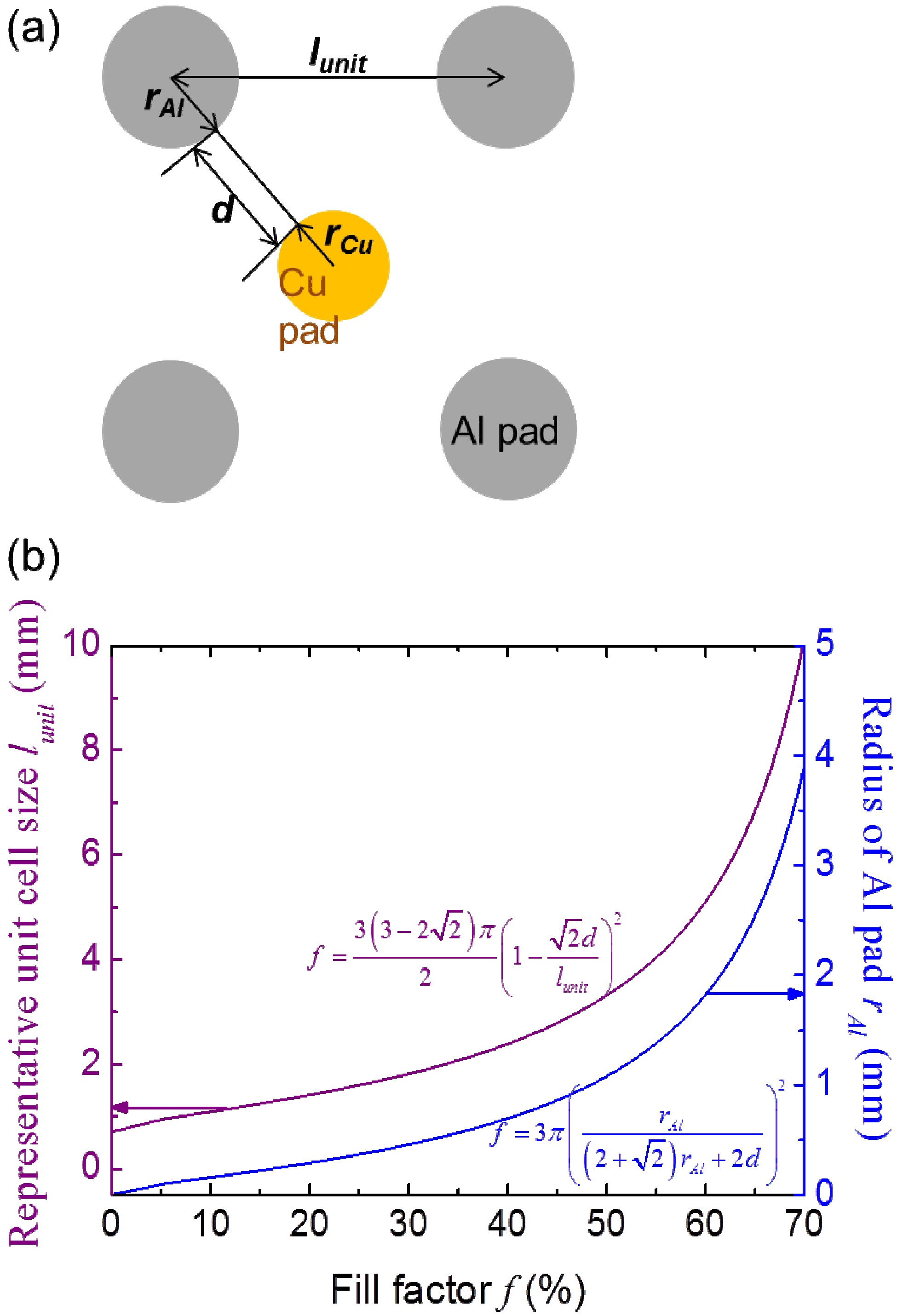

Supplementary Figure S9 | Layout and design concern on the geometric parameters of the Al and Cu pads. The layout of Al and Cu pads is shown in (a), and the dependences of fill factor on the size of a representative unit cell and the radius of the Al pad are illustrated in (b). The offset distance (*d*) is set to be 0.5 mm in the model to avoid possible short circuits as the battery is stretched.

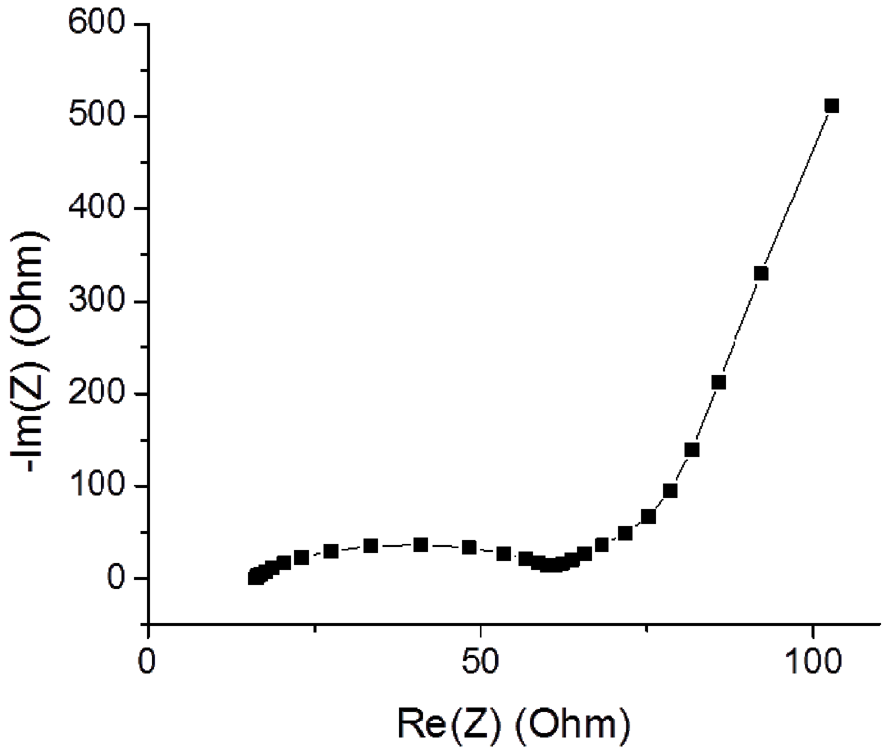

Supplementary Figure S10 | Nyquist impedance plot for the pouch type stretchable battery. The frequency is in the range of 1 MHz to 10 mHz, and the a.c. perturbation amplitude is 10 mV.

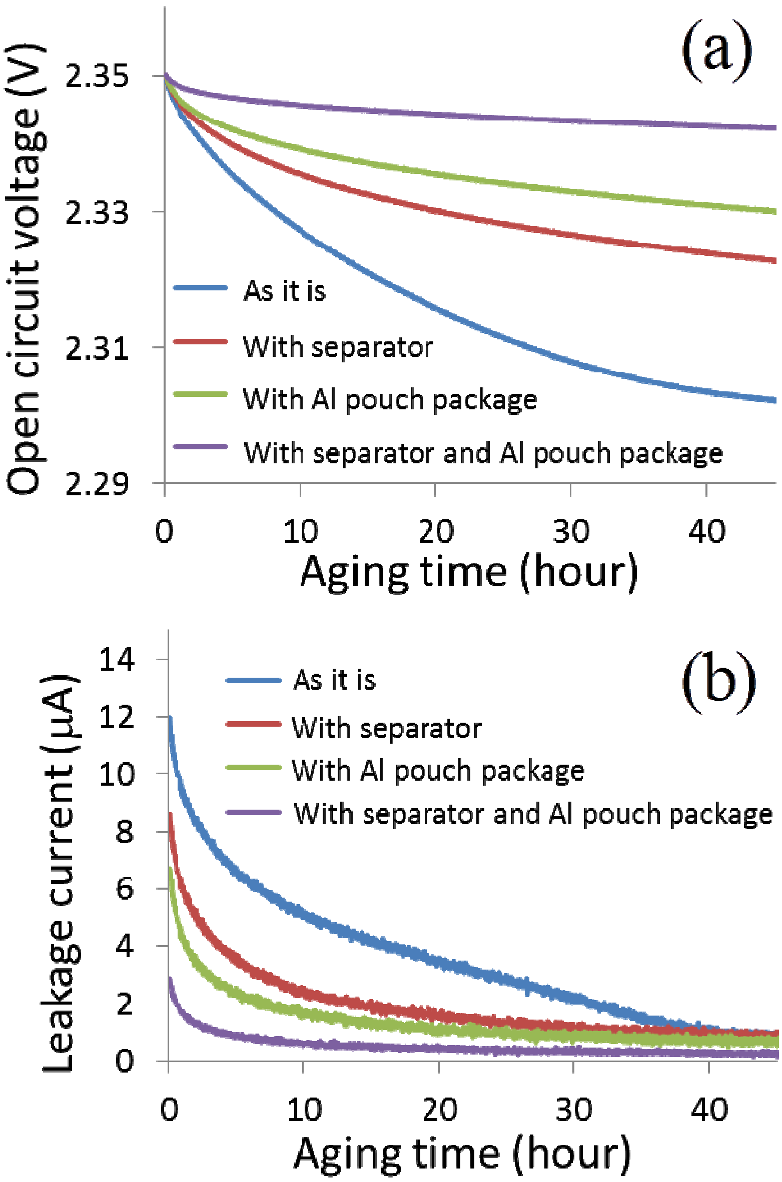

Supplementary Figure S11 | Leakage current evaluation for batteries in various configurations. (a) Open circuit voltage decay curves and (b) leakage current curves, measured at room temperature.

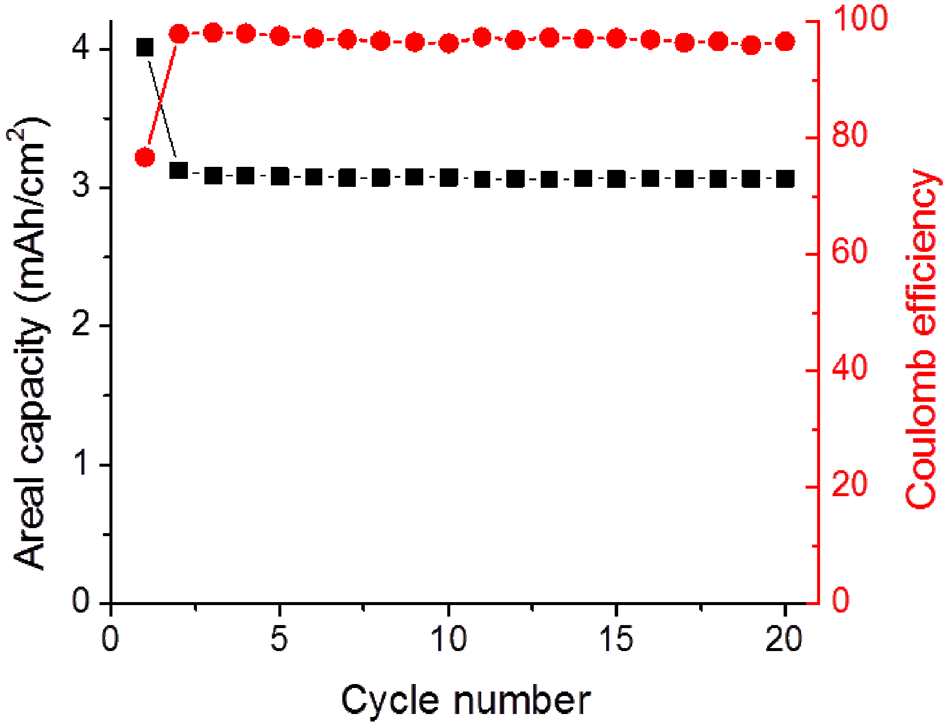

Supplementary Figure S12 | Electrochemical performance of the battery materials in coil cell geometries. Capacity retention (black) and coulombic efficiency (red) over 20 cycles with a cutoff voltage of 2.5-1.6 V with exactly the same slurries and the capacitance matched cathode and anode geometries.

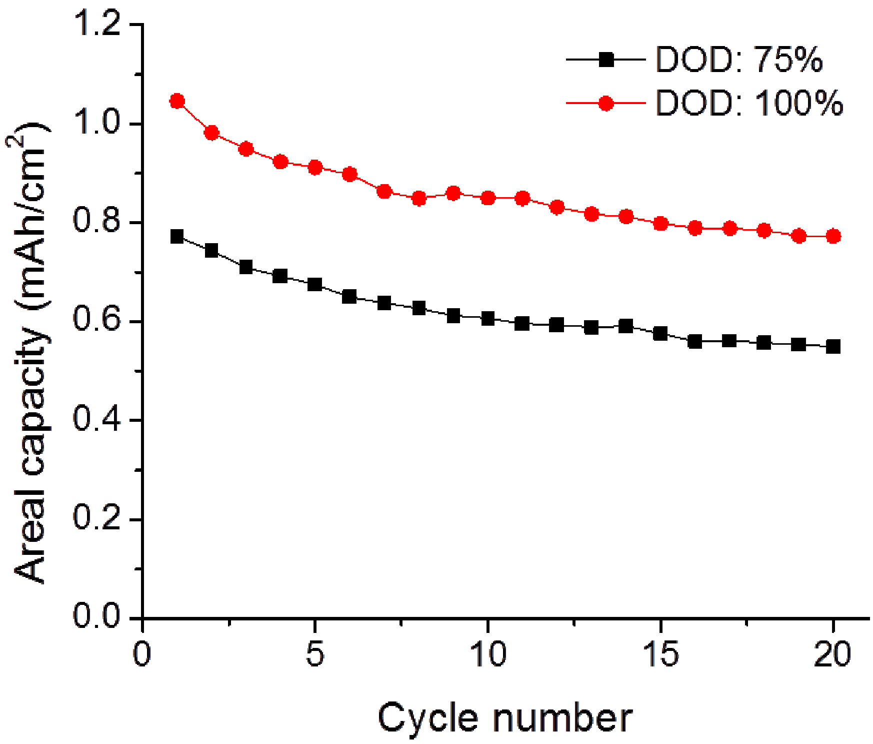

Supplementary Figure S13 | Cycling performance with different depths of discharge. Capacity retention curves with depth of discharge of 100% (red curve, cut-off voltage of 1.60-2.50 V) and ~75% (black curve, cut-off voltage of 2.25-2.50 V).

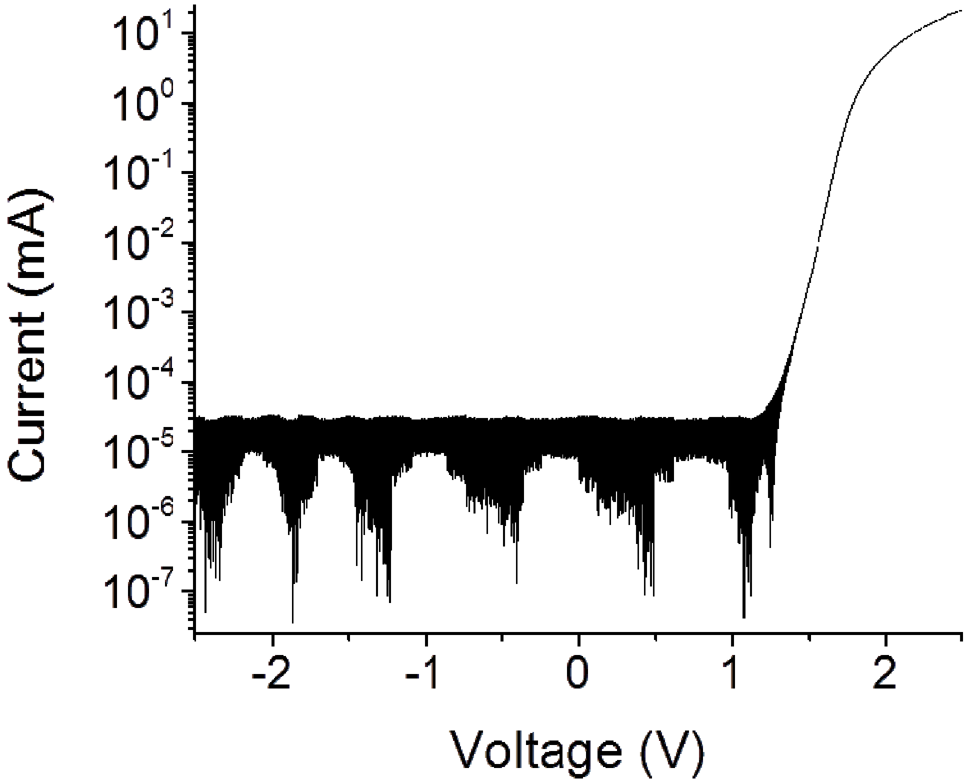

Supplementary Figure S14 | I-V curve of the commercial red light emitting diode. It shows its turn on voltage at around 1.7 V.

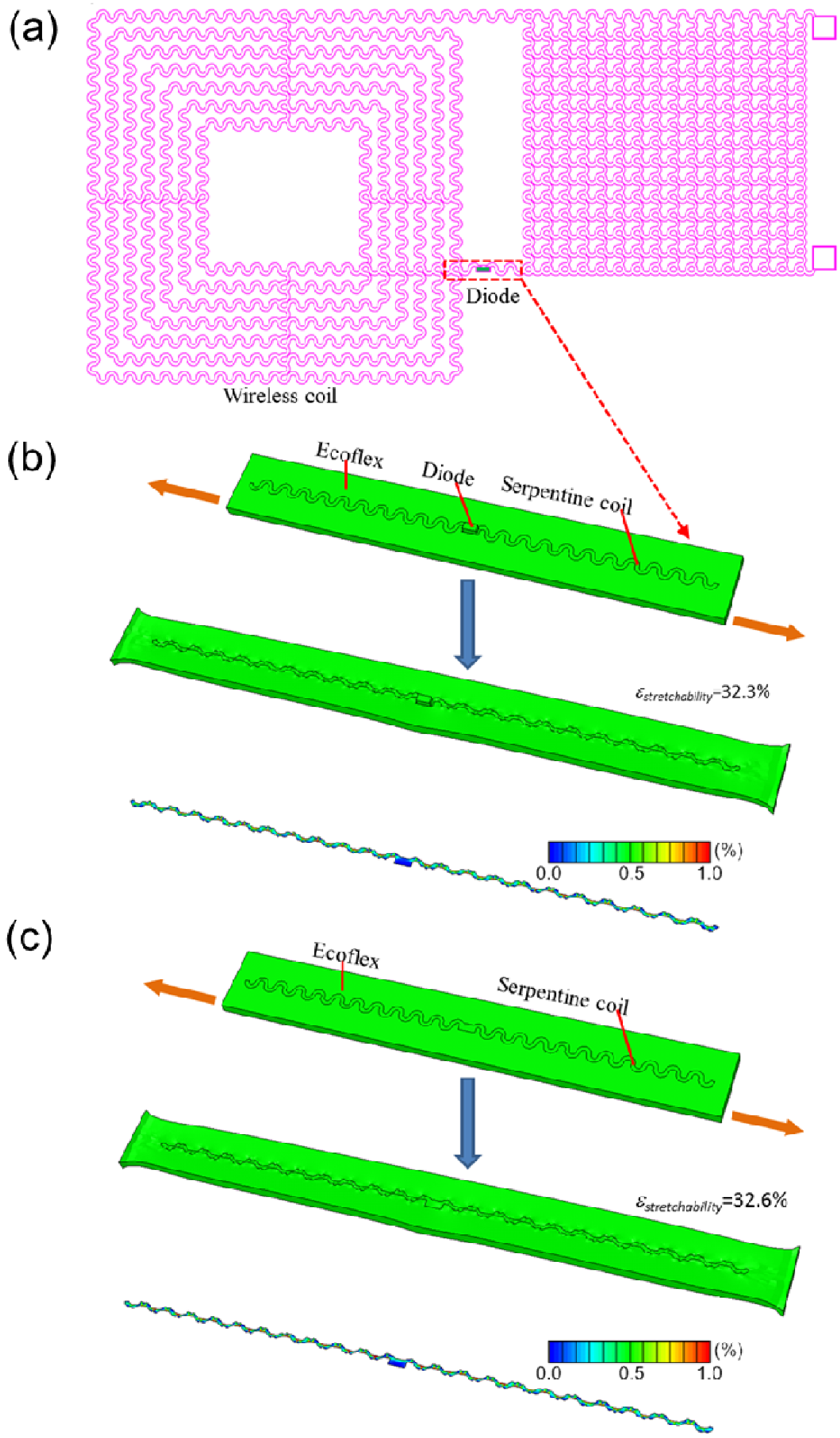

Supplementary Figure S15 | Influence of the discrete diode on the stretchability of the wireless recharging system. (a) Schematic illustration of the layout of a wireless recharging system; (b) Calculated deformation and distribution of maximum principal strain under an applied strain of 32.3%, for a representative component of the wireless coil, with both the discrete diode and serpentine interconnect; (c) Calculated deformation and distribution of maximum principal strain under an applied strain of 32.6%, for a representative component of the wireless coil, with only the serpentine interconnect.

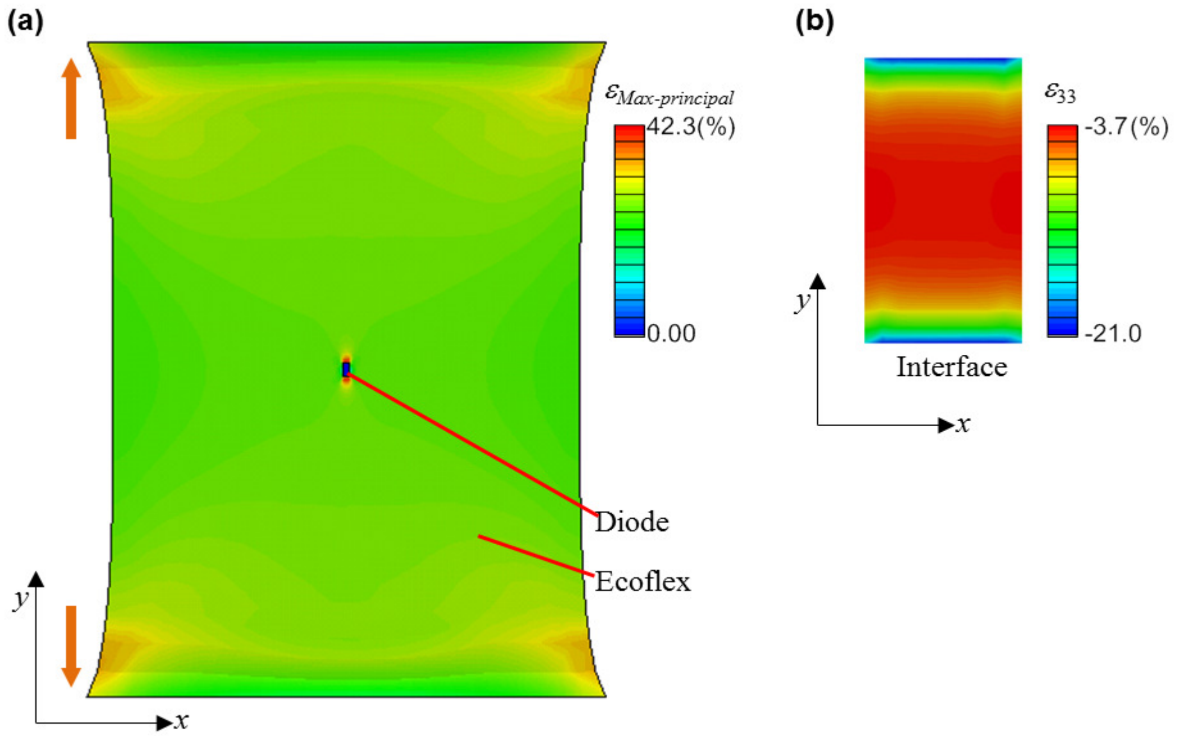

Supplementary Figure S16 | Finite element simulations on a discrete diode on a large Ecoflex substrate under stretching. Calculated distribution of (a) maximum principal strain in the whole structure, and (b) substrate normal strain (e_{33}) at the diode/substrate interface, when the system is stretched by 30% along the vertical direction.

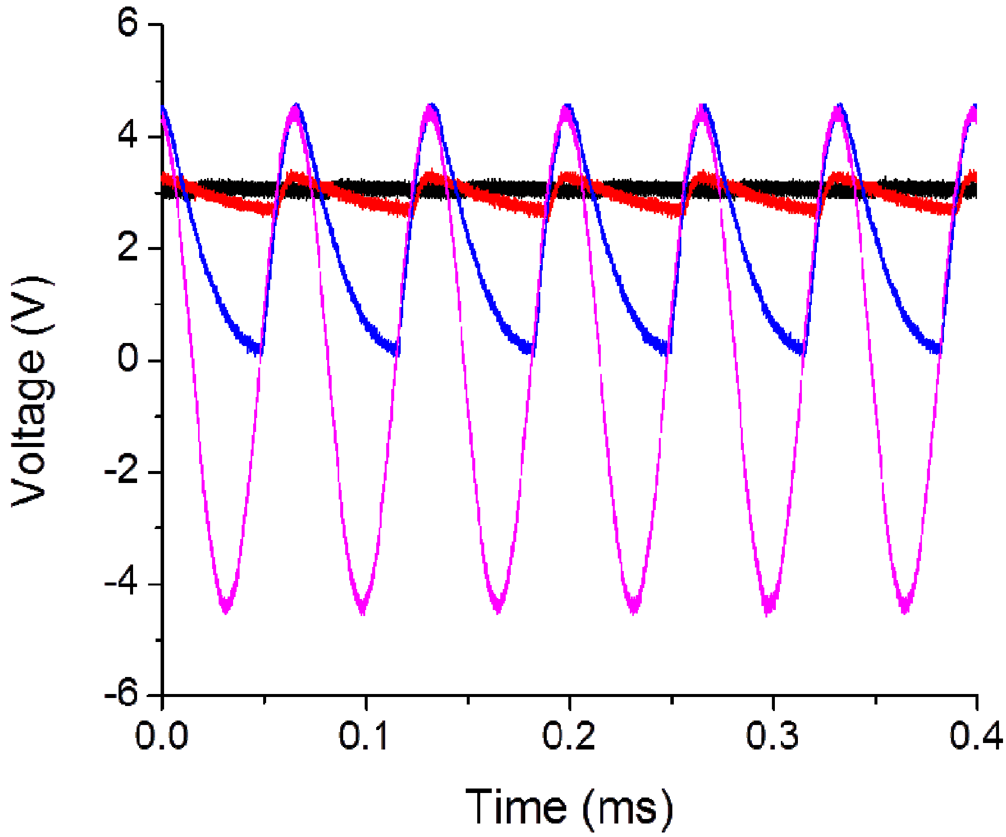

Supplementary Figure S17 | The input and output electrical characteristics of the wireless charging systems. The Schottky diode rectifies the alternating voltage input from the functional generator (pink curve), to yield a rectified output (blue curve), which oscillates nominally from 0 V to 4.6 V. The parallel 1.7 nF capacitor integrates this oscillation to give a current source with a behavior closer to direct current (red curve). Increasing the capacitance (e.g. 17 nF) further smooths the current (black curve).

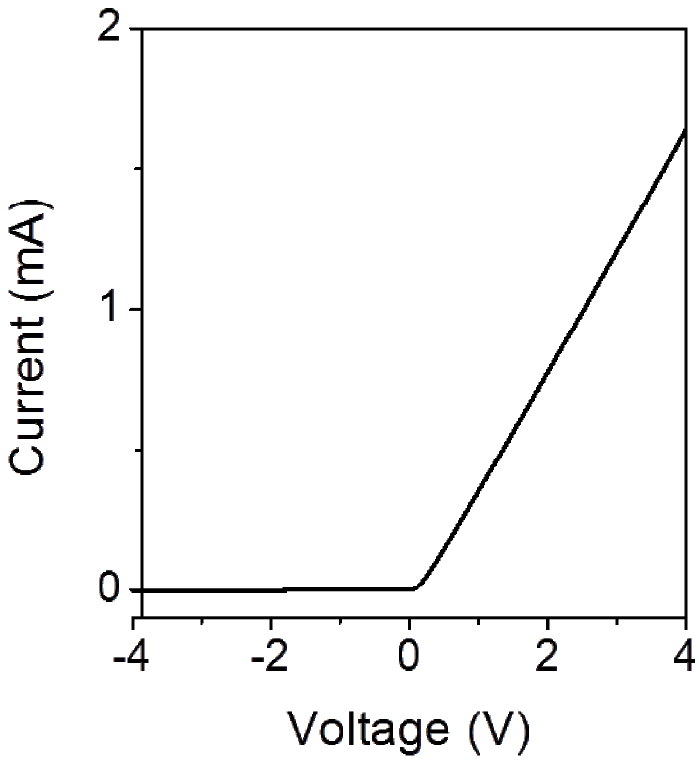

Supplementary Figure S18 | I-V curve of the wireless coil with the rectifying chip. The series resistance of the wireless coil is about 2.3 KΩ.

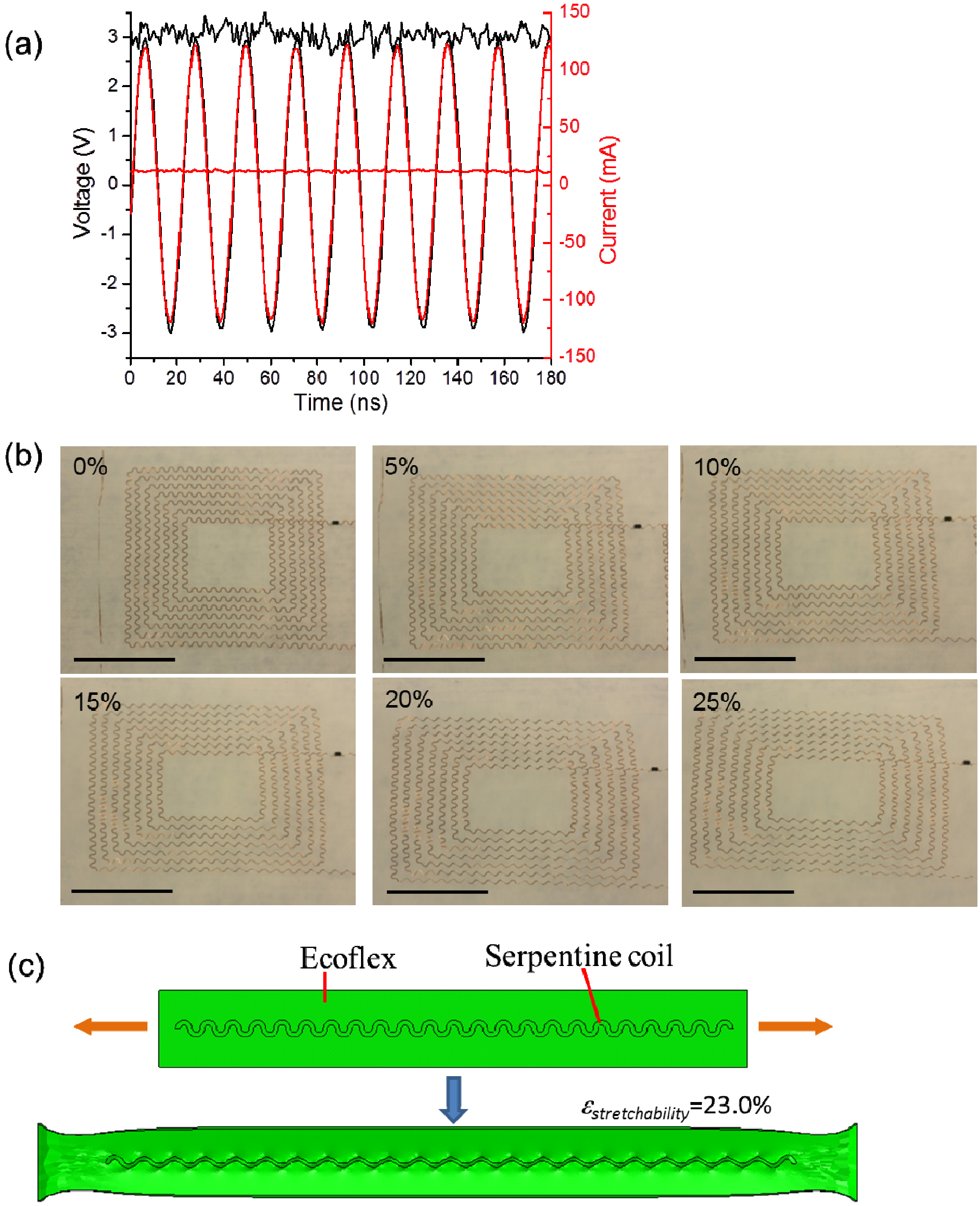

Supplementary Figure S19 | Wireless coil performance using thickner copper foil. (a) Input and output voltages (black) and currents (red) of the wireless coil 18 μm thick copper foil. (b) Optical micrographs of a 7 μm thick Cu coil at different levels of applied uniaxial strain. The scale bars are all 1 cm. (c) Finite element analysis of stretching of a segment of a serpentine coil with a thickness of 7 μm.

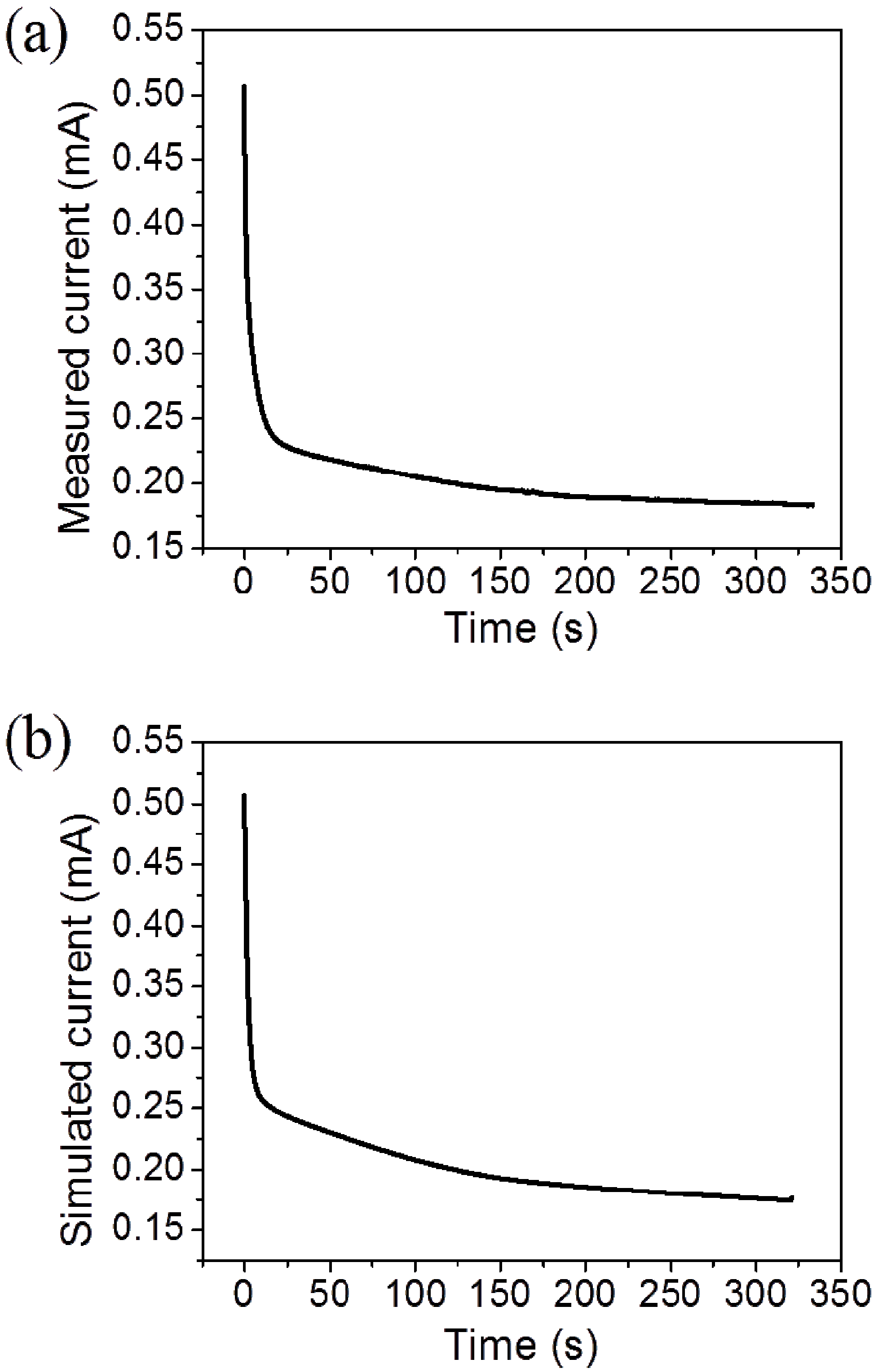

Supplementary Figure S20│Experimental and simulated charging current. Comparison between the measured current change and the simulated result in the wireless coil charging circuit to the battery.

Supplementary Methods

Fabrication of a stretchable encapsulating layer, consisting of a buckled sheet of Al/PI on a silicone substrate

The first step involved fabrication of a trilayer of PMMA/PI/Al on a silicon substrate, using procedures similar to those employed for the Al battery electrodes. Photolithography with AZ5214E and wet etching the Al defined the lateral dimensions of the PI/Al sheet. Next, oxygen plasma etching (300 mT, 20 sccm O_2, 200 W for 5 mins) removed the PI layer in the exposed regions. Immersion in hot acetone partially removed the underlying PMMA layer, thereby allowing the entire structure to be retrieved from the silicon wafer onto the surface of a piece of water soluble tape (3M, Inc.). Electron beam evaporation of Ti (5 nm) / SiO_2 (50 nm) formed backside coatings. On a separate substrate, 500 μm thick silicone sheets (Ecoflex, Smooth-On) were prepared, then removed and prestrained biaxially to a level of ~30% and then fixed by lamination onto a glass slide. The silicone surface was activated by exposure to UV-indued ozone for 5 mins. Laminating the PI/Al bilayer onto this surface led to strong bonding, upon contact. The water soluble tape was removed by immersing the substrate in tap water for overnight. Peeling the entire assembly away from the glass slide released the prestrain, and led to an expected pattern of buckling. In this configuration, the overall system can be stretched to strains as large as those equal to the prestrain.

Mechanical analyses of "island-bridge" self-similar electrode structures: FEA

Full three-dimensional (3D) FEA is adopted to analyze the postbuckling behaviors of "island-bridge" self-similar electrodes structures under stretching and compression. Due to the structural periodicity of the electrode, a representative unit cell was studied, and its detailed geometry is shown in Supplementary Fig. S1. The circular island of the electrode is mounted on a post (height 250 μm) molded on the surface of a silicone substrate (ecoflex; thickness 500 μm). The metal interconnect (thickness 0.6 μm), is encased, top and bottom, by a thin layer of polyimide (PI, thickness 1.2 μm for each layer). The elastic modulus (E) and Poisson's ratio (v) are $E_{ecoflex}$=0.06 MPa and $v_{ecoflex}$=0.49 for ecoflex; E_{Cu}=119 GPa and v_{Cu}=0.34 for copper; E_{Al}=70 GPa and v_{Al}=0.35 for aluminum; and E_{PI}=2.5 GPa and v_{PI}=0.34 for PI. Eight-node 3D solid elements and four-node shell elements were used for the ecoflex and self-similar electrode, respectively, and refined meshes were adopted to ensure the accuracy. The evolution of deformed configurations with applied strains are obtained from FEA for both stretching and compression, as shown in Fig. 2 and Supplementary Fig. S8, respectively. Good agreement between FEA and experiment results can be found. Here, we take the case of copper as a demonstration of the buckling profiles. The results for the aluminium layer are similar. For the comparison of stretchability and revesibility between self-similar and serpentine interconnects (Supplementary Fig. S7), the key geometrical parameters are kept the same, including the total length (l_{total}=16.77 mm), span (L=1.6 mm), amplitude (h=0.4 mm), width (w=30 μm), and thickness (t=3.0 μm). The aluminium interconnect (thickness 0.6 μm) is encased by two thin layers of polyimide (thickness 1.2 μm for each layer). Supplementary Fig. S7 demonstrates that over the entire range of stretching from 0% to ~800%, the strain level of the self-similar interconnect is always lower than the serpentine one. The stretchability (809%) and reversibility (528%) of the self-similar design, are higher than those ($\varepsilon_{stretchability}$=682%, $\varepsilon_{reversibility}$=284%) of the simple serpentine design.

Battery leakage current analysis

The leakage current arises from three sources. The first source is current through the reverse biased Schottky diode. This current is ~0.2 μA, and is relatively constant throughout the lifetime of the battery. Schottky diodes with smaller reverse current are available; such devices can reduce this contribution to the leakage.

The second source is the internal ohmic self-discharge current between the slurry disks at the anode and cathode. This contribution arises from finite electronic conductivity of the electrolyte and any parasitic physical contacts between the slurry disks at the cathode and anode. These losses can be dramatically reduced by electrolyte materials with enhanced purity and implementing separators. New experiments reveal the latter effects quantitatively. Supplementary Figs. S11a and b show the voltage decay and leakage current curves for otherwise similar batteries with and without a commercial separator (Celgard). This component reduces the capacity loss from 161 μA·h to 88 μA·h in 44 hours.

The third source is from current produced by Faradaic effects, including shuttle reactions associated with impurities in the slurry materials, residual oxygen and/or moisture. Improving the air-impermeability of the packaging materials can reduce currents that arise from such reactions. New experiments show that sealing the battery in an Al pouch (which can be configured in a wrinkled configuration to allow stretching, according to strategies outlined in the original manuscript) reduces the capacity loss from 161 μA·h to 62 μA·h. Combining the separator and the Al pouch packaging, suppresses the capacity loss to 23 μA·h. Supplementary Fig. S11 summarizes all of these findings.

Discrete Schottky diode stretching behavior analysis

From a practical standpoint, we observe no significant constraints on the overall mechanical properties of the integrated system, due to the comparatively small size of the diode. In particular, although the Schottky diode, which is encapsulated in epoxy which has a modulus of ~4.0 GPa, is effectively more than 4 orders of magnitude larger than that of substrate (made of Ecoflex, with a modulus of ~60 KPa), its dimensions (length 0.62 mm, width 0.32 mm, and height 0.31 mm) represent only a few percent (~2%) of the overall size (~30 mm × ~20 mm) of the wireless system. Experimentally, we observe that the system is robust to stretching up to ~30% and beyond.

To study these effects quantitatively, we carried out full, three dimensional finite element simulations that examine the influence of the diode on the stretchability of the coil in the integrated system, as in Supplementary Fig. S15a. Results in Supplementary Fig. S15b and S15c, indicate that: (1) The decrease in stretchability is modest, from 32.6% to 32.3%, when the diode is included and (2) The strain in the diode (i.e. the epoxy) is very small (< 0.15%, much smaller than the strain needed to induce fracture), even when the overall system is stretched by 32.3%.

The normal interface strain is also important. Supplementary Fig. S16a shows the distributions of maximum principal strains in a large Ecoflex substrate with a diode mounted in its center, for stretching to 30%. Supplementary Fig. S16b illustrates the distribution of the substrate normal strain at the diode/substrate interface. The normal interface strain in this case is negative, corresponding to compressive strain at the interface. This outcome, which is consistent with theoretical predictions based on energy release rates at an interface crack, minimizes the propensity for delamination.

<u>Coil resistance effect on the wireless power transfer efficiency</u>

The coil resistance/qualify factor is a critical parameter that dictates the efficiency. In additional experiments to illustrate the effects, we replaced the 600 nm thick gold serpentine coils with otherwise similar ones fabricated with copper at increased thicknesses. The results show that coils formed using a 7 μm thick copper film (Dupont) have total resistances of 185 Ω, and generate a received power of 30.8 mW with an input power of 179 mW (at a distance of 1 mm, similar to the previously reported results). The corresponding efficiency is 17.2%, which represents more than a factor of three improvement over the original, gold coils (4.9%). Further reducing the coil resistance to 38 Ω by using 18 μm thick copper foil (MTI Corp.) improves the received power to 36.2 mW, and the efficiency to 20.2%. See Supplementary Fig. S19a.

These increases in thickness, and therefore power transfer efficiencies, lead to changes in the essential mechanics associated with stretching. In particular, as the thickness increases, the stretchability decreases. The coil with thickness of 7 μm offers a good balance between efficiency and mechanical deformability, with ability to accommodate strains of ~25%. Images at various levels of strain appear in Fig. S19b, which agree with well the finite element analysis results in terms of both the maximum uniaxial strain and the geometry of the coil serpentines (Supplementary Fig. S19c).

Modeling of the charging current in the wireless power transmission circuit

The charging circuit can be described using the model below:

$$U_0 = U(t) + L\frac{dI(t)}{dt} + I(t)R \tag{1}$$

Here U_0 is the charging source of 3 volts voltage. L and R are the associated inductance and the resistance of the circuit. $U(t)$ is the time dependent readout of the voltmeter and $I(t)$ is the time dependent readout of an ammeter.

A program has been developed to simulate the I-V curve based on the partial differential equation (1). The simulated time dependent current $I_s(t)$ based on $U(t)$ is compared with measured $I(t)$, and the results are shown in Supplementary Fig. S20.

The program used to simulate the current:

```
#include<iostream.h>
#include<stdio.h>
#include<stdlib.h>
#include<math.h>
#include<time.h>
#define tim 3500
#define start 265
float curre[tim];
float nihe[tim];
float test[tim];
float voll[tim];

FILE *fp;

int main()
{
        int i,j,k;

   fp=fopen("Cur.txt","r");
        for(i=0;i<tim;i++)
```

```
            {
                        fscanf(fp,"%f",&curre[i]);
                        curre[i]=-curre[i];
                        cout<<curre[i]<<endl;
            }
fclose(fp);

fp=fopen("Vol.txt","r");
for(i=0;i<tim;i++)
            {
                        fscanf(fp,"%f",&voll[i]);
                        cout<<voll[i]<<endl;
            }
fclose(fp);

double coef1;
double coef2;

coef2=curre[1]/(voll[1]-voll[0]);

cout<<coef2<<endl;
test[0]=curre[0];
test[start]=curre[start];

double coef1th;
double maxh=1000000000;
double coef2th;
for(coef2=0;coef2<0.04; coef2=coef2+0.0001)
{
            cout<<coef2<<endl;
            for(coef1=0.94; coef1<=0.96; coef1=coef1+0.0001)
            {
            // cout<<coef1<<endl;
            for(i=start+1;i<tim;i++)
            {
                        test[i]=coef1*test[i-1]+(3-(voll[i]+voll[i-1])*0.5)*coef2;
            }
            double poi=0;
            for(i=start;i<tim;i++)
            {
                        poi+=(test[i]-curre[i])*(test[i]-curre[i]);
            }
            if(poi<maxh)
            {
                        coef1th=coef1;
                        coef2th=coef2;

                        maxh=poi;
                        for(int j=0;j<tim;j++)
                        {
                                    nihe[j]=test[j];
                        }
            }
            }
}
cout<<coef1th<<endl;
cout<<coef2th<<endl;
cout<<maxh<<endl;

fp=fopen("nihe.txt","w");
for(i=0;i<tim;i++)
{
```

```
		fprintf(fp, "%f", -nihe[i]);
		fprintf(fp, "\n");
	}
	fclose(fp);

	fp=fopen("canshu.txt","w");

	fprintf(fp, "%f", coef1th);
	fprintf(fp, "\n");

	fprintf(fp, "%f", coef2th);
	fprintf(fp, "\n");

	fclose(fp);
	return(1);
}
```